

Chiral Dynamics Near Intra- and Inter-Band Exceptional Points under Dissipative Spin-Orbital-Angular-Momentum Coupling

Bo-Wen Liu,¹ Ke-Ji Chen,^{1,*} Fan Wu,^{2,†} and Wei Yi^{3,4,5,6,‡}

¹Key Laboratory of Quantum States of Matter and Optical Field Manipulation of Zhejiang Province, Department of Physics, Zhejiang Sci-Tech University, 310018 Hangzhou, China

²Fujian Key Laboratory of Quantum Information and Quantum Optics, College of Physics and Information Engineering, Fuzhou University, Fuzhou, Fujian 350108, China

³Laboratory of Quantum Information, University of Science and Technology of China, Hefei 230026, China

⁴Anhui Province Key Laboratory of Quantum Network,

University of Science and Technology of China, Hefei, 230026, China

⁵CAS Center For Excellence in Quantum Information and Quantum Physics, Hefei 230026, China

⁶Hefei National Laboratory, University of Science and Technology of China, Hefei 230088, China

(Dated: January 8, 2026)

We study the parametric chiral dynamics of atoms under dissipative spin-orbital-angular-momentum coupling (SOAMC). With atoms confined in the ring-shaped potential of the Laguerre-Gaussian Raman beams, the SOAMC not only couples the atomic center-of-mass angular momentum to the hyperfine spins, but also mixes different bands in the radial direction. This gives rise to a series of exceptional points of two types, the intra-band and the inter-band. Leveraging the topology of the spectral Riemann surface close to these exceptional points, we demonstrate the path-dependent chiral transfer of atoms to the higher-lying bands, by evolving the system along closed loops in the parameter space. Specifically, we illustrate two distinct scenarios, characterized by different mechanisms, where the atoms can be transferred to designated SOAMC-dressed bands. Our work demonstrates the rich exceptional structure in atom gases under dissipative SOAMC, and offers a novel route toward populating higher bands.

PACS numbers:

Synthetic spin-orbital-angular-momentum coupling (SOAMC) represents a latest addition to the toolbox of quantum simulation in cold atoms [1–3]. Like the synthetic spin-orbit coupling before it [4–9], SOAMC couples the atomic center-of-mass motion to their internal hyperfine-spin degrees of freedom, and, by modifying the single-particle dispersion [10–13], enables the simulation of topological matter [14, 15], interaction-induced phase transitions [16–20], vortices in superfluids [21, 22], as well as exotic few- and many-body pairing states [3, 23, 24].

Alternatively, the single-particle dispersion can also be dramatically modified by dissipation. For instance, the eigenspectrum of a system can be made complex by introducing non-Hermiticity, often through post selection in the open-system dynamics. A whole new range of non-Hermitian features, such as the exceptional points (EPs) [25, 26], the non-Hermiticity enriched symmetry [27–29], and non-Hermitian skin effects [30, 31] then give rise to complex spectral geometries and intriguing dynamics that have stimulated tremendous activities of late [32–46]. Outstanding examples include the chiral state transfer near EPs in lossy cold atoms [40, 46], and topological edge states associated with the non-Bloch topology [42]. Nevertheless, while the quantized angular momenta and multiple radial modes typical of SOAM-coupled gases have much potential in quantum control and engineering, the spectral geometry and its dynamic consequences under a non-Hermitian SOAMC have yet

to be explored.

In this work, we study the parametric chiral dynamics of cold atoms under a non-Hermitian SOAMC. The SOAMC couples both the quantized angular momenta and radial modes (or bands) of atoms in a ring-shaped potential, leading to a complicated spectral Riemann surface with a series of intra- and inter-band EPs in the parameter space. We show that these EPs are useful for the chiral population of higher band. Specifically, by varying system parameters along a closed loop near the EPs (dubbed EP encircling), the atoms can end up in a designated high-lying band, provided the loop is traversed with the required chirality. Based on the geometry of the Riemann surface, we demonstrate two distinct scenarios, wherein such chiral state transfer can be achieved either non-adiabatically or adiabatically, and involving multiple EPs. Our study is experimentally accessible, and has further implications for quantum control and simulation with cold atoms.

Model. — We consider an ensemble of non-interacting two-component atoms confined in the two-dimensional $x - y$ plane. The SOAMC is generated by a two-photon Raman process using a pair of co-propagating Laguerre-Gaussian beams carrying angular momenta $-l_1\hbar$ and $-l_2\hbar$, as illustrated in Fig. 1(a). The resulting Raman field features an inhomogeneous Raman coupling $\Omega(r)$ and a phase winding $e^{-2il\theta}$ with $2l = l_1 - l_2$ in the polar coordinates $\mathbf{r} = (r, \theta)$. Following Ref. [40], we con-

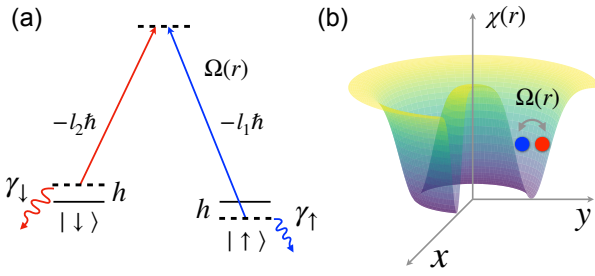


FIG. 1: (a) Schematic level structure with spin-dependent atom loss. (b) The ac Stark shift of the Raman process $\chi(r)$ provides the ring-shaped confinement, while the Raman coupling $\Omega(r)$ drives transitions between distinct hyperfine states.

sider laser-assisted spin-dependent loss, with rates $\gamma_{\uparrow,\downarrow}$. The effective non-Hermitian Hamiltonian becomes (under a gauge transformation) [2]: $H_0 = \int d\mathbf{r} \psi^\dagger \mathcal{H}_s \psi$, where $\psi = (\psi_\uparrow, \psi_\downarrow)^T$ denotes the two-component atomic field and \mathcal{H}_s is (up to a constant term)

$$\mathcal{H}_s = -\frac{\hbar^2}{2M} \frac{1}{r} \frac{\partial}{\partial r} \left(r \frac{\partial}{\partial r} \right) + \frac{(L_z - \hbar \sigma_z)^2}{2Mr^2} + \chi(r) + \Omega(r) \sigma_x - \omega \sigma_z, \quad (1)$$

with M the atom mass and σ_j ($j = x, y, z$) the Pauli matrices. Here $\omega = h - i\gamma$, with h the two-photon detuning and $\gamma = (\gamma_\downarrow - \gamma_\uparrow)/2$. Under the Raman-assisted SOAMC, the hyperfine spin states are coupled to the atomic orbital angular momentum through the term $-\hbar L_z \sigma_z / (Mr^2)$ with $L_z = -i\hbar \partial / \partial \theta$. The ac Stark shift $\chi(r)$ of the Raman beams provides a ring-shaped trapping potential [see Fig. 1(b)]. The Raman coupling and the ac Stark shift take the forms $\Omega(r) = \Omega_0 I(r)$ and $\chi(r) = \chi_0 I(r)$, respectively, with Ω_0 and χ_0 their corresponding strengths. The intensity profile is $I(r) = (\sqrt{2}r/w)^{|l_1|+|l_2|} e^{-2r^2/w^2}$, and w the beam waist. For numerical calculations below, an isotropic hard-wall boundary with radius R is introduced.

The eigenspectrum of Hamiltonian (1) can be numerically obtained under an appropriate choice of basis [see Supplemental Material]. Here, we adopt an alternative approach to clarify the underlying physics. Since $[L_z, \mathcal{H}_s] = 0$, we expand the field operator as $\psi_\sigma(\mathbf{r}) = \sum_{m,n} \varphi_{mn\sigma}(r) \Theta_m(\theta) a_{mn\sigma}$, with $\Theta_m(\theta) = e^{im\theta} / \sqrt{2\pi}$ and $a_{mn\sigma}$ the corresponding annihilation operator. The radial function satisfies $K_\sigma(\mathbf{r}) \varphi_{mn\sigma}(r) \Theta_m(\theta) = \epsilon_{mn\sigma} \varphi_{mn\sigma}(r) \Theta_m(\theta)$, where $K_\sigma(\mathbf{r}) = -\frac{\hbar^2}{2M} \left[\frac{1}{r} \frac{\partial}{\partial r} \left(r \frac{\partial}{\partial r} \right) + \frac{1}{r^2} \left(\frac{\partial}{\partial \theta} - i l \tau \right)^2 \right] + \chi_0 I(r)$, and $\tau = +1(-1)$ for $\sigma = \uparrow(\downarrow)$. Here $m \in \mathbb{Z}$ and $n \in \mathbb{N}$ denote the angular and radial quantum numbers, respectively. For a sufficiently deep ac Stark potential [see Fig. 1(b)], adjacent radial levels for a given angular quantum number m are well separated, we therefore identify n as an effective band index

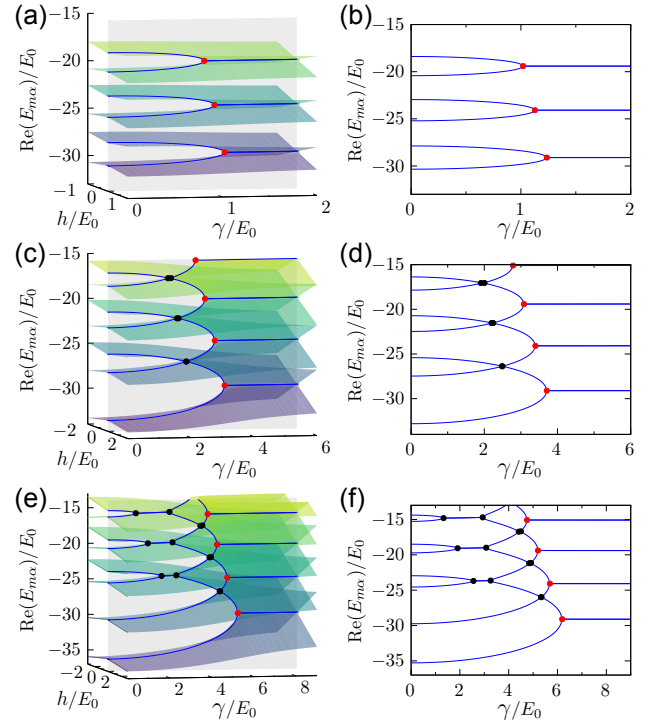


FIG. 2: Riemann surfaces of the real components of the eigenspectra, parameterized by h and γ in the $m = 0$ sector. The right panels show the cross sections of the Riemann surfaces on the plane of $h = 0$. The blue solid lines indicate the branch cuts, and red (black) dots mark intra-(inter-)band EPs. (a)(b) $\Omega_0/E_0 = 0.27$, (c)(d) $\Omega_0/E_0 = 0.82$, and (e)(f) $\Omega_0/E_0 = 1.37$. Other parameters are fixed as $l_1 = 4$, $l_2 = -4$, $w = 3a$, $R = 15a$, and $\chi_0/E_0 = -6.85$. We take $E_0 = \hbar^2 / (Ma^2)$ as the unit of energy.

($n = 0, 1, 2, 3, \dots$ corresponding to s, p, d, f, \dots). The Hamiltonian can then be written as $H_0 = \sum_m H_m$, with

$$H_m = \sum_{n\sigma} \left[\epsilon_{mn\sigma} - \omega \tau \right] a_{mn\sigma}^\dagger a_{mn\sigma} + \sum_{nn'} \left[\Omega_{n\uparrow, n'\downarrow}^\dagger a_{mn\uparrow}^\dagger a_{mn'\downarrow} + h.c. \right], \quad (2)$$

where $\Omega_{n\sigma, n'\sigma'}^m = \Omega_0 \int r dr \varphi_{mn\sigma} I(r) \varphi_{mn'\sigma'}$ couples spin components in different radial bands. Diagonalizing H_m yields the eigenvalues $E_{m\alpha}$, where $\alpha \in \mathbb{Z}^+$ labels the SOAMC-dressed bands, ordered in accordance with the band indices in the presence of SOAMC. Specifically, $\alpha = 2n + 1$ ($\alpha = 2n + 2$) denotes the lower (upper) branch of the n th dressed band. We show in Fig. 2 typical real components of the eigenspectra in the $m = 0$ sector; whereas those in other m sectors are demonstrated in the Supplemental Material. As illustrated in Fig. 2(a)(b), under a weak Raman coupling, different dressed bands are indeed well separated, but each features an intra-band EP (marked in red). With increasing Raman coupling strength, different dressed bands hybridize, leading to the emergence of inter-band EPs [see Fig. 2(c)(d),

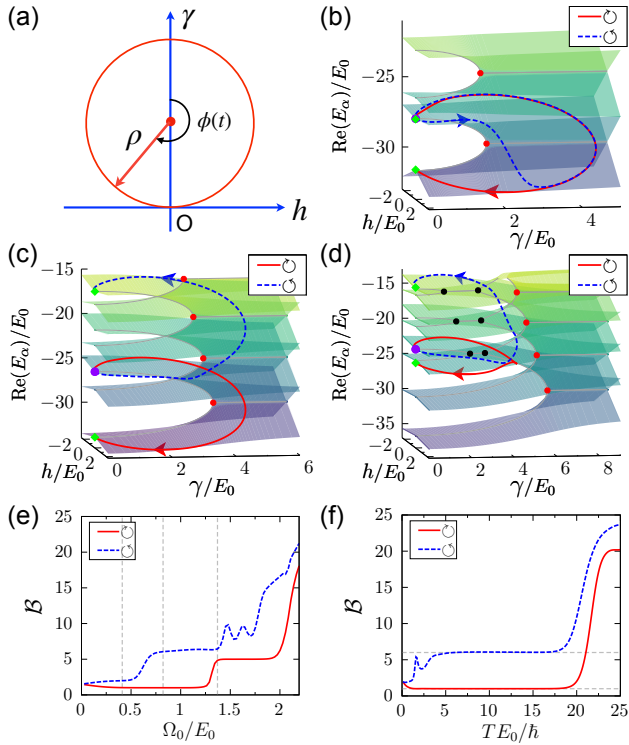


FIG. 3: (a) Schematic evolution of h and γ . Here, $\phi(t) = \pm 2\pi t/T + \pi$, where $+$ ($-$) corresponds to clockwise (counterclockwise) encircling. (b)(c)(d) The spectral trajectories under clockwise (\odot , red solid) and counterclockwise (\ominus , blue dashed) encircling at different Raman coupling Ω_0 . The values $\Omega_0/E_0 = 0.41, 0.82$ and 1.37 correspond to panels (b), (c) and (d), respectively. Purple dots indicate the initial points, green diamonds the final points, and the gray curves show the branch cuts. (e) The relation between \mathcal{B} and the Raman coupling strength Ω_0 . The gray dashed lines correspond to the cases shown in (b)(c)(d). (f) The relation between \mathcal{B} and the encircling time T . The gray dashed lines ($\mathcal{B} = 1$ and $\mathcal{B} = 6$) denote the lower dressed s and the upper dressed d bands. For panels (b)-(e), we fix $TE_0/\hbar = 7.5$, while for panel (f), $\Omega_0/E_0 = 0.82$. All other parameters are identical to those in Fig. 2, with $\rho/E_0 = 2.34$.

marked in black; see Supplemental Material for the imaginary bands]. The number of EPs increases with the coupling strength [see Fig. 2(e)(f)], and the coexistence of intra- and inter-band EPs gives rise to a complicated spectral Riemann surface, which have rich dynamic implications.

Chiral dynamics.— We study chiral dynamics over closed paths in the parameter space via the time-dependent Schrödinger equation $i\hbar\partial_t\psi = \mathcal{H}_s(t)\psi$, where

$$\mathcal{H}_s(t) = \sum_{\sigma} K_{\sigma}(\mathbf{r}) + \Omega_0 I(r)\sigma_x - \omega(t)\sigma_z, \quad (3)$$

with $\omega(t) = h(t) - i\gamma(t)$ indicating the closed path in the parameter space. Under $\mathcal{H}_s(t)$, dynamics in different m sectors are decoupled, and their Riemann surfaces

possess similar structures [see Supplemental Material]. We therefore focus on the $m = 0$ sector, without loss of generality. Therein, the dynamics are governed by $i\hbar\partial_t\Phi(t) = \mathcal{H}(t)\Phi(t)$, where $\mathcal{H}(t)$ and $\Phi(t)$ denote the non-Hermitian Hamiltonian and the time-evolved state in the $m = 0$ sector, respectively [see Supplemental Material for their explicit expressions].

To characterize the chiral dynamics, we expand the time-evolved state as $\Phi(t) = \sum_{\alpha} c_{\alpha}(t)r_{\alpha}(t)$, where $c_{\alpha}(t)$ are the coefficients and $r_{\alpha}(t)$ are the instantaneous eigenstates with eigenvalues $E_{\alpha}(t)$. Chirality is revealed through the spectral trajectory $\mathcal{E}(t)$ and the final-state band index \mathcal{B} , defined respectively as

$$\mathcal{E}(t) = \frac{\sum_{\alpha} E_{\alpha}(t)|c_{\alpha}(t)|^2}{\sum_{\alpha} |c_{\alpha}(t)|^2}, \quad (4)$$

$$\mathcal{B} = \frac{\sum_{\alpha} \alpha |c_{\alpha}(T)|^2}{\sum_{\alpha} |c_{\alpha}(T)|^2}, \quad (5)$$

where T is the time for the system to traverse the closed path. Intuitively, if the final state predominantly occupies a single dressed band with index α , $\mathcal{B} \approx \alpha$ is close to an integer.

As illustrated in Fig. 3(a), we initialize the system at the branch cut of the upper s dressed band (with $\alpha = 2$), and parameterize the path as

$$h(t) = \rho \sin \phi(t), \quad \gamma(t) = \rho + \rho \cos \phi(t), \quad (6)$$

where $\phi(t) = \pm 2\pi t/T + \pi$ (with $t \in [0, T]$), and the sign \pm denotes the chirality (clockwise or counterclockwise) of the encircling dynamics. Here ρ represents the encircling radius.

Figure 3(b)(c)(d) show the spectral trajectories, against the Riemann surface, with different Ω_0 , for the clockwise (red) and counterclockwise (blue) encircling directions, respectively. In the case with weak Raman couplings where different dressed bands are well separated, the initial state evolves primarily within its own band while traversing different Riemann sheets [see Fig. 2(b)]. As is typical for EP encircling [44, 45], different encircling directions yield different final states. Here, in a clockwise encircling, the time evolution adiabatically follows the Riemann surface, and the state flips to the lower branch of the dressed s band on returning to the initial parameters. By contrast, in a counterclockwise encircling, a non-adiabatic jump occurs, and the system returns to the initial state at time T . The observed chiral dynamics is attributed to the imaginary components of the eigenspectrum, with the time-evolved state tending toward the eigenstate with $\text{Im}(E_{\alpha}(t)) > 0$ during the evolution [32–34, 46].

This picture is modified when the Raman-induced band hybridization becomes significant. As shown in Fig. 3(c) for $\Omega_0/E_0 = 0.82$, while the trajectory remains in the dressed s band under the clockwise encircling, under a counterclockwise encircling, the trajectory shifts

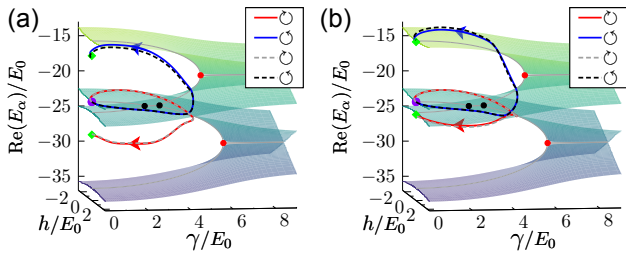


FIG. 4: Comparison of trajectories calculated from the effective and full Hamiltonians, for (a) $TE_0/\hbar = 4$ and (b) $TE_0/\hbar = 7.5$. The red (blue) solid lines denote the results of the two-band Hamiltonian for clockwise (counterclockwise) encircling, while the dark-gray (black-gray) dashed lines show the corresponding full-band results. Here, $\Omega_0/E_0 = 1.37$ and $\rho/E_0 = 2.34$. Other parameters are the same as those in Fig. 2.

from the upper dressed s to d bands. More remarkably, further increasing the Raman coupling strength would change the final state in both directions. This is shown in Fig. 3(d), where the clockwise (counterclockwise) encircling ends in the lower (upper) dressed d band. These observations suggest that the chiral dynamics and its final states are tunable in our setup.

In Fig. 3(e), we plot the final-state band index \mathcal{B} as a function of the Raman coupling strength for both encircling directions. For $\Omega_0/E_0 \in (0.25, 0.5)$, the chiral dynamics reproduces similar results as in a generic two-level system [44, 45]. Here the geometry close to the intra-band EP dominates. For $\Omega_0/E_0 \in (0.75, 1.25)$, the chiral dynamics is similar to the case in Fig. 3(c), clockwise encirclings transfer the initial state from the upper to the lower dressed s band, while counterclockwise encircling ends up in the upper dressed d band. For even strong Raman couplings, clockwise encircling breaks adiabaticity as well, transferring the initial state from the upper dressed s band to the lower dressed d band. Finally, for sufficiently large Ω_0 , \mathcal{B} increases significantly, as final states in both directions occupy higher-lying dressed bands. This is due to the fact that the eigenvalues of these higher-lying bands feature larger imaginary components.

We also examine the encircling process with a fixed path but with increasing encircling time T . As shown in Fig. 3(f), for intermediate encircling time $TE_0/\hbar \in (5, 17.5)$, and a counterclockwise rotation, the final state dominantly occupies the upper dressed d band, with $\mathcal{B} = 6$. By contrast, the final state flips to the lower dressed s band (with $\mathcal{B} = 1$) under a clockwise rotation. Again, in the long-time limit, the occupation of the higher-lying dressed bands are exponentially occupied due to their larger imaginary eigenvalue components.

Effective Model.— As discussed above, except at long times, the overall chiral dynamics involve only two bands,

and hence can be captured by an effective two-band model. Owing to the steep ac Stark potential, we expand $\psi_\sigma(\mathbf{r}) = \sum_{m,n=s,d} \varphi_{mn\sigma}(r) \Theta_m(\theta) a_{mn\sigma}$, restricting the basis to the s and d bands. This choice is motivated by two considerations: the initial state occupies the upper dressed s band; and the coupling between the s and d bands is much stronger than that between the s and p bands. Within these factors, we derive an effective Hamiltonian in the $m = 0$ sector, where $H_{\text{eff}} = \Phi^\dagger \mathcal{H}_{\text{eff}} \Phi$ and

$$\mathcal{H}_{\text{eff}} = \begin{pmatrix} \epsilon_{s\uparrow} - \omega & \Omega_{s\uparrow,s\downarrow} & 0 & \Omega_{s\uparrow,d\downarrow} \\ \Omega_{s\uparrow,s\downarrow} & \epsilon_{s\downarrow} + \omega & \Omega_{d\uparrow,s\downarrow} & 0 \\ 0 & \Omega_{d\uparrow,s\downarrow} & \epsilon_{d\uparrow} - \omega & \Omega_{d\uparrow,d\downarrow} \\ \Omega_{s\uparrow,d\downarrow} & 0 & \Omega_{d\uparrow,d\downarrow} & \epsilon_{d\downarrow} + \omega \end{pmatrix}. \quad (7)$$

Here $\Phi = (a_{s\uparrow} \ a_{s\downarrow} \ a_{d\uparrow} \ a_{d\downarrow})^T$. This effective Hamiltonian captures both the static and dynamical properties of the system. To examine the validity of the effective Hamiltonian, we compare the trajectories calculated from dynamics under the effective and full Hamiltonians. As shown in Fig. 4, the results agree remarkably well at different intermediate time scales.

Under the effective model, the impact of the encircling time T , particularly in the non-adiabatic evolution in Fig. 3(d), can be well explained. For example, under an intermediate encircling time T [see Fig. 4(b)], the final state in either direction is transferred to the dressed d band. This behavior arises from the different imaginary eigenvalue components of the bands. These can be obtained by analyzing Eq. (7). When the coupling between the s and d bands vanishes, Eq. (7) reduces to $\mathcal{H}_{\text{eff}} = \mathcal{M}_s \oplus \mathcal{M}_d$, where

$$\mathcal{M}_n = \begin{pmatrix} \epsilon_{n\uparrow} - \omega & \Omega_{n\uparrow,n\downarrow} \\ \Omega_{n\uparrow,n\downarrow} & \epsilon_{n\downarrow} + \omega \end{pmatrix}. \quad (8)$$

The eigenvalues of Eq. (8) are $E_\pm = \epsilon_n \pm \sqrt{\omega^2 + (\Omega_{n\uparrow,n\downarrow})^2}$, with $\epsilon_{n\uparrow} = \epsilon_{n\downarrow} = \epsilon_n$ for $m = 0$. Since $|\Omega_{s\uparrow,s\downarrow}| > |\Omega_{d\uparrow,d\downarrow}|$, the imaginary eigenvalue components of the d band is larger than that of the s band based on Eq. (8). Hence, when increasing the encircling time T , there exists a time window in which the occupation of the d band becomes dominant, as observed in Fig. 3(d).

Encircling multiple EPs.— The tunable chiral preparation of states in high-lying bands demonstrated thus far hinges upon the presence of intra-band EPs, and often involve non-adiabatic processes. But with the emergence of inter-band EPs, one can design an adiabatic pathway toward higher-lying bands on the Riemann surface, making use of both types of EPs.

For this purpose, we consider the path in Fig. 5(a), which consists of several loops parameterized by

$$h(t) = \rho_k \sin \phi_k(t), \quad \gamma(t) = \rho_k + \rho_k \cos \phi_k(t), \quad (9)$$

where $\phi_k(t) = (-1)^k 2\pi \left(t - \sum_{k=1}^{k-1} T_{k-1} \right) / T_k + \pi$ with $k = 1, 2, 3$ and $T_0 = 0$. Physically, we start from the

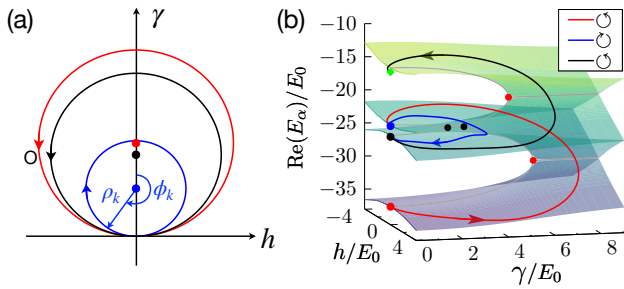


FIG. 5: (a) Schematic of the designed loops. The red, blue and black circles denotes the first, second and third loops with distinct encircling radius, and the corresponding dots mark their origins. (b) Spectral trajectories of the encircling. Here, $\rho_{k=1,2,3} = (4, 2.05, 3.5)E_0$, $T_{k=1,2,3} = (1.35, 3.2, 1.1)\hbar/E_0$ with $\Omega_0/E_0 = 1.37$. Other parameters are the same as those in Fig. 2.

lower dressed s band, and the first loop is chosen to encircle the intra-band EP in the dressed s band [see Fig. 5(b)]; the second loop encircles the inter-band EP between the dressed s and d bands; and the third loop encircles the intra-band EP of the dressed d band. Figure 5(b) shows the resulting spectral trajectory based on the effective Hamiltonian [see Supplemental Material for the comparison between results from the effective and full Hamiltonians]. As expected, an adiabatic evolution along the path, including both clockwise and counterclockwise sectors, leaves the system in the upper branch of a higher band. Note that while we illustrate the adiabatic chiral state transfer using the s and d bands, the design can be extended to high-lying bands (for instance between p and f bands).

Discussion.— We have illustrated the parametric chiral state transfer of atoms under the dissipative SOAMC, designed according to the rich exceptional structure of the system. The chiral dynamics is useful for the path-dependent preparation of atoms in the high-lying bands. While our results are readily accessible in a non-interacting condensate subject to a dissipative SOAMC, we expect the consideration of nonlinear contributions of condensate interactions would further enrich the exceptional structure and chiral dynamics.

Acknowledgement.— We acknowledge fruitful discussions with Konghao Sun. This work is supported by the Natural Science Foundation of China (Grants No. 12104406, 12374479, 12204105). K.C. acknowledges support by Zhejiang Provincial Natural Science Foundation (Grant No. ZCLMS25A0401) and the startup grant of Zhejiang Sci-Tech University (Grant No. 21062338-Y). W.Y. acknowledges support from the Innovation Program for Quantum Science and Technology (Grant No. 2021ZD0301904).

- * Electronic address: chenkeji2010@gmail.com
† Electronic address: t21060@fzu.edu.cn
‡ Electronic address: wyz@ustc.edu.cn
- [1] H.-R. Chen, K.-Y. Lin, P.-K. Chen, N.-C. Chiu, J.-B. Wang, C.-A. Chen, P.-P. Huang, S.-K. Yip, Y. Kawaguchi, and Y.-J. Lin, Spin-Orbital-Angular-Momentum Coupled Bose-Einstein Condensates, *Phys. Rev. Lett.* **121**, 113204 (2018).
 - [2] D. Zhang, T. Gao, P. Zou, L. Kong, R. Li, X. Shen, X.-L. Chen, S.-G. Peng, M. Zhan, H. Pu, and K. Jiang, Ground-State Phase Diagram of a Spin-Orbital-Angular-Momentum Coupled Bose-Einstein Condensate, *Phys. Rev. Lett.* **122**, 110402 (2019).
 - [3] S.-G. Peng, K. Jiang, X.-L. Chen, K.-J. Chen, P. Zou, and L. He, Spin-orbital-angular-momentum-coupled quantum gases, *AAPPS Bulletin* **32**, 36 (2022).
 - [4] V. Galitski and I. B. Spielman, Spin-orbit coupling in quantum gases, *Nature (London)* **494**, 49 (2013).
 - [5] N. Goldman, G. Juzeliūnas, and P. Öhberg, and I. B. Spielman, Light-induced gauge fields for ultracold atoms, *Rep. Prog. Phys.* **77**, 126401 (2014).
 - [6] H. Zhai, Degenerate quantum gases with spin-orbit coupling: a review, *Rep. Prog. Phys.* **78**, 026001 (2015).
 - [7] W. Yi, W. Zhang, and X. Cui, Pairing superfluidity in spin-orbit coupled ultracold Fermi gases, *Sci. China Phys. Mech. Astron.* **58**, 1 (2015).
 - [8] J. Zhang, H. Hu, X. J. Liu, and H. Pu, Fermi gases with synthetic spin-orbit coupling, *Annu. Rev. Cold At. Mol.* **2**, 81 (2014).
 - [9] L. Zhang and X. J. Liu, Spin-orbit coupling and topological phases for ultracold atoms, in *Synthetic Spin-Orbit Coupling in Cold Atoms*, edited by W. Zhang, W. Yi, and C. A.R. Sá Melo (World Scientific, Singapore, 2018), pp.1–87.
 - [10] M. DeMarco and H. Pu, Angular spin-orbit coupling in cold atoms, *Phys. Rev. A* **91**, 033630 (2015).
 - [11] C. Qu, K. Sun, and C. Zhang, Quantum phases of Bose-Einstein condensates with synthetic spin-orbital-angular-momentum coupling, *Phys. Rev. A* **91**, 053630 (2015).
 - [12] K. Sun, C. Qu, and C. Zhang, Spin-orbital-angular-momentum coupling in Bose-Einstein condensates, *Phys. Rev. A* **91**, 063627 (2015).
 - [13] L. Chen, H. Pu, and Y. Zhang, Spin-orbit angular momentum coupling in a spin-1 Bose-Einstein condensate, *Phys. Rev. A* **93**, 013629 (2016).
 - [14] L. Chen, Y. Zhang, and H. Pu, Spin-Nematic Vortex States in Cold Atoms, *Phys. Rev. Lett.* **125**, 195303 (2020).
 - [15] K.-J. Chen, F. Wu, L. He, and W. Yi, Angular topological superfluid and topological vortex in an ultracold Fermi gas, *Phys. Rev. Res.* **4**, 033023 (2022).
 - [16] X.-L. Chen, S.-G. Peng, P. Zou, X.-J. Liu, and H. Hu, Angular stripe phase in spin-orbital-angular-momentum coupled Bose condensates, *Phys. Rev. Res.* **2**, 033152 (2020).
 - [17] K.-J. Chen, F. Wu, J. Hu, and L. He, Ground-state phase diagram and excitation spectrum of a Bose-Einstein condensate with spin-orbital-angular-momentum coupling, *Phys. Rev. A* **102**, 013316 (2020).
 - [18] Y. Duan, Y. M. Bidasyuk, and A. Surzhykov, Symmetry breaking and phase transitions in Bose-Einstein condensates with spin-orbital-angular-momentum coupling,

- Phys. Rev. A **102**, 063328 (2020).
- [19] Y. M. Bidasyuk, K. S. Kovtunenکو, and O. O. Prikhodko, Fine structure of the stripe phase in ring-shaped Bose-Einstein condensates with spin-orbital-angular-momentum coupling, Phys. Rev. A **105**, 023320 (2022).
- [20] R. Cao, J. Han, J. Wu, J. Yuan, L. He, and Y. Li, Quantum phases of spin-orbital-angular-momentum-coupled bosonic gases in optical lattices, Phys. Rev. A **105**, 063308 (2022).
- [21] K.-J. Chen, F. Wu, S.-G. Peng, W. Yi, and L. He, Generating Giant Vortex in a Fermi Superfluid via Spin-Orbital-Angular-Momentum Coupling, Phys. Rev. Lett. **125**, 260407 (2020).
- [22] L.-L. Wang, A.-C. Ji, Q. Sun, and J. Li, Exotic Vortex States with Discrete Rotational Symmetry in Atomic Fermi Gases with Spin-Orbital-Angular-Momentum Coupling, Phys. Rev. Lett. **126**, 193401 (2021).
- [23] Y. Han, S.-G. Peng, K.-J. Chen, and W. Yi, Molecular state in a spin-orbital-angular-momentum coupled Fermi gas, Phys. Rev. A **106**, 043302 (2022).
- [24] X.-L. Chen, A. Chen, and S.-G. Peng, Two atoms in a harmonic trap with spin-orbital-angular-momentum coupling, Phys. Rev. Res. **6**, 033200 (2024).
- [25] C. M. Bender, Making sense of non-Hermitian Hamiltonians, Rep. Prog. Phys. **70**, 947 (2007).
- [26] M.-A. Miri and A. Alù, Exceptional Points in Optics and Photonics, Science **363**, eaar7709 (2019).
- [27] Y. Ashida, Z. Gong, and M. Ueda, Non-Hermitian physics, Adv. Phys. **69**, 249 (2020).
- [28] K. Kawabata, K. Shiozaki, M. Ueda, and M. Sato, Symmetry and Topology in Non-Hermitian Physics, Phys. Rev. X **9**, 041015 (2019).
- [29] E. J. Bergholtz, J. C. Budich, and F. K. Kunst, Exceptional Topology of Non-Hermitian Systems, Rev. Mod. Phys. **93**, 015005 (2021).
- [30] S. Yao and Z. Wang, Edge states and topological invariants of non-Hermitian systems, Phys. Rev. Lett. **121**, 086803 (2018).
- [31] F. K. Kunst, E. Edvardsson, J. C. Budich, and E. J. Bergholtz, Biorthogonal Bulk-Boundary Correspondence in Non-Hermitian Systems, Phys. Rev. Lett. **121**, 026808 (2018).
- [32] J. Doppler, A. A. Mailybaev, J. Böhm, U. Kuhl, A. Girschikm, F. Libisch, T. J. Milburn, P. Rabl, N. Moiseyev, and S. Rotter, Dynamically Encircling an Exceptional Point for Asymmetric Mode Switching, Nature (London) **537**, 76 (2016).
- [33] X.-L. Zhang, S. Wang, B. Hou, and C. T. Chan, Dynamically encircling exceptional points: In situ control of encircling loops and the role of the starting point, Phys. Rev. X **8**, 021066 (2018).
- [34] Ş. K. Özdemir, S. Rotter, F. Nori, and L. Yang, Parity-time symmetry and exceptional points in photonics, Nat. Mater. **18**, 783 (2019).
- [35] W.-Q. Liu, Y. Wu, C.-K. Duan, X. Rong, and J.-F. Du, Dynamically encircling an exceptional point in a real quantum system, Phys. Rev. Lett. **126**, 170506 (2021).
- [36] Q. Song, M. Odeh, J. Zuniga-Perez, B. Kante, and P. Genevet, Plasmonic topological metasurface by encircling an exceptional point, Science **373**, 1133 (2021).
- [37] W. Chen, M. Abbasi, Y. N. Joglekar, and K. W. Murch, Quantum Jumps in the Non-Hermitian Dynamics of a Superconducting Qubit, Phys. Rev. Lett. **127**, 140504 (2021).
- [38] W. J. Chen, M. Abbasi, B. Ha, S. Erdamar, Y. N. Joglekar, and K. W. Murch, Decoherence Induced Exceptional Points in a Dissipative Superconducting Qubit, Phys. Rev. Lett. **128**, 110402 (2022).
- [39] L. Ding, K. Shi, Y. Wang, Q. Zhang, C. Zhu, L. Zhang, J. Yi, S. Zhang, X. Zhang, and W. Zhang, Information retrieval and eigenstate coalescence in a non-Hermitian quantum system with anti- \mathcal{PT} symmetry, Phys. Rev. A **105**, L010204 (2022).
- [40] Z. Ren, D. Liu, E. Zhao, C. He, K. K. Pak, J. Li, and G.-B. Jo, Chiral control of quantum states in non-Hermitian spin-orbit-coupled fermions, Nat. Phys. **18**, 385 (2022).
- [41] H. Nasari, G. Lopez-Galmitche, H. E. Lopez-Aviles, A. Schumer, A. U. Hassan, Q. Zhong, S. Rotter, P. LiKamWa, D. N. Christodoulides, and M. Khajavikhan, Observation of chiral state transfer without encircling an exceptional point, Nature (London) **605**, 256 (2022).
- [42] Q. Liang, D. Xie, Z. Dong, H. Li, H. Li, B. Gadway, W. Yi, and B. Yan, Dynamic signatures of non-Hermitian skin effect and topology in ultracold atoms, Phys. Rev. Lett. **129**, 070401 (2022).
- [43] H. Qi, Y. Li, X. Wang, Y. Li, X. Li, X. Wang, X. Hu, and Q. Gong, Dynamically encircling exceptional points in different Riemann sheets for orbital angular momentum topological charge conversion, Phys. Rev. Lett. **132**, 243802 (2024).
- [44] T. J. Milburn, J. Doppler, C. A. Holmes, S. Portolan, S. Rotter, and P. Rabl, General Description of Quasidiabatic Dynamical Phenomena near Exceptional Points, Phys. Rev. A **92**, 052124 (2015).
- [45] A. U. Hassan, B. Zhen, M. Soljačić, M. Khajavikhan, and D. N. Christodoulides, Dynamically Encircling Exceptional Points: Exact Evolution and Polarization State Conversion, Phys. Rev. Lett. **118**, 093002 (2017).
- [46] K. Sun and W. Yi, Chiral state transfer under dephasing, Phys. Rev. A **108**, 013302 (2023).

Supplemental Material for “Chiral Dynamics Near Intra- and Inter-Band Exceptional Points under Dissipative Spin-Orbital-Angular-Momentum Coupling”

In this Supplemental Material, we present details of the eigenspectrum of a non-Hermitian Hamiltonian obtained from both the direct basis expansion and the full-band expansion. We also provide the chiral dynamical formalism and compare the adiabatic encircling results from the effective two-band model with those from full-band calculations.

EIGENSPECTRUM OF A NON-HERMITIAN HAMILTONIAN

Direct basis expansion

As discussed in the main text, the eigenspectrum of \mathcal{H}_s , as shown in Eq. (1), can be obtained directly by choosing an appropriate basis. Specifically, the eigenvalues are determined by diagonalizing the following Schrödinger equation,

$$\begin{pmatrix} K_{\uparrow}(\mathbf{r}) - \omega & \Omega(r) \\ \Omega(r) & K_{\downarrow}(\mathbf{r}) + \omega \end{pmatrix} \begin{pmatrix} u_{\eta}(\mathbf{r}) \\ v_{\eta}(\mathbf{r}) \end{pmatrix} = E_{\eta} \begin{pmatrix} u_{\eta}(\mathbf{r}) \\ v_{\eta}(\mathbf{r}) \end{pmatrix}, \quad (\text{S1})$$

where $E_{\eta} \in \mathbb{C}$ are the eigenvalues with η labeling the energy index, and $u_{\eta}(\mathbf{r})$ and $v_{\eta}(\mathbf{r})$ are the corresponding eigenstate components. Here, $\omega = h - i\gamma$, where h denotes the two-photon detuning and γ characterizes the atom loss. In Eq. (S1), $K_{\sigma}(\mathbf{r}) = -\frac{\hbar^2}{2M} \left[\frac{1}{r} \frac{\partial}{\partial r} \left(r \frac{\partial}{\partial r} \right) + \frac{1}{r^2} \left(\frac{\partial}{\partial \theta} - i l \tau \right)^2 \right] + \chi(r)$ with $\tau = +1(-1)$ for $\sigma = \uparrow(\downarrow)$. As shown in the main text, the Raman coupling $\Omega(r)$ and the ac Stark shift $\chi(r)$ take the forms $\Omega_0 I(r)$ and $\chi_0 I(r)$, where Ω_0 and χ_0 denote their corresponding strengths, respectively. The intensity profile is given by $I(r) = (\sqrt{2}r/w)^{|l_1|+|l_2|} e^{-2r^2/w^2}$ with w the beam waist. Here, we impose an isotropic hard-wall boundary of radius R in realistic numerical calculations.

Considering $[L_z, \mathcal{H}_s] = 0$, with $L_z = -i\hbar\partial/\partial\theta$, and imposing an isotropic two-dimensional hard-wall boundary condition, the radial wave function $f_{m\alpha\sigma}(r)$ can be expanded in terms of the Bessel functions, where α labels the radial eigenmode. Accordingly, the eigenstate of \mathcal{H}_s can be written as

$$u_{\eta}(\mathbf{r}) = f_{m\alpha\uparrow}(r)\Theta_m(\theta) = \sum_p c_{m\alpha\uparrow}^p R_{p,m-l}(r)\Theta_m(\theta), \quad (\text{S2})$$

$$v_{\eta}(\mathbf{r}) = f_{m\alpha\downarrow}(r)\Theta_m(\theta) = \sum_p c_{m\alpha\downarrow}^p R_{p,m+l}(r)\Theta_m(\theta), \quad (\text{S3})$$

where $R_{pm}(r) = \sqrt{2}J_m(z_{pm}r/R)/[RJ_{m+1}(z_{pm})]$ and $\Theta_m(\theta) = e^{im\theta}/\sqrt{2\pi}$. Here $R_{pm}(r)$ is the radial wave function of the two-dimensional hard-wall potential, and z_{pm} is the p th zero of $J_m(x)$ with $p \in \mathbb{Z}^+$. Substitute Eq. (S2) and (S3) into Eq. (S1), each m becomes decoupled and in each m sector, we have

$$\sum_{p'} \begin{pmatrix} K_{\uparrow}^{pp'} & \Omega_{p,m-l}^{p',m+l} \\ \Omega_{p,m+l}^{p',m-l} & K_{\downarrow}^{pp'} \end{pmatrix} \begin{pmatrix} c_{m\alpha\uparrow}^{p'} \\ c_{m\alpha\downarrow}^{p'} \end{pmatrix} = E_{m\alpha} \begin{pmatrix} c_{m\alpha\uparrow}^p \\ c_{m\alpha\downarrow}^p \end{pmatrix}, \quad (\text{S4})$$

where $K_{\sigma,m-l\tau}^{pp'}$ and $\Omega_{p,m}^{p',m'}$ have the following forms,

$$K_{\sigma,m-l\tau}^{pp'} = \left(\frac{\hbar^2 z_{p,m-l\tau}^2}{2MR^2} - \omega\tau \right) \delta_{pp'} + \chi_0 \int r dr R_{p,m-l\tau}(r) R_{p',m-l\tau}(r), \quad (\text{S5})$$

$$\Omega_{p,m}^{p',m'} = \Omega_0 \int r dr R_{p,m}(r) I(r) R_{p',m'}(r). \quad (\text{S6})$$

Diagonalizing Eq. (S4) yields the eigenvalues and eigenfunctions. Figure S1 shows the real parts of the eigenspectra for different m at a fixed Raman coupling. A common feature is the emergence of exceptional points (EPs), and the overall Riemann-surface structures remain similar across different m , despite variations in the EP values.

While the above approach is straightforward for obtaining the eigenspectrum of \mathcal{H}_s , its physical meaning can become ambiguous, particularly when extended to dynamics. To clarify the physics, we adopt an alternative approach.

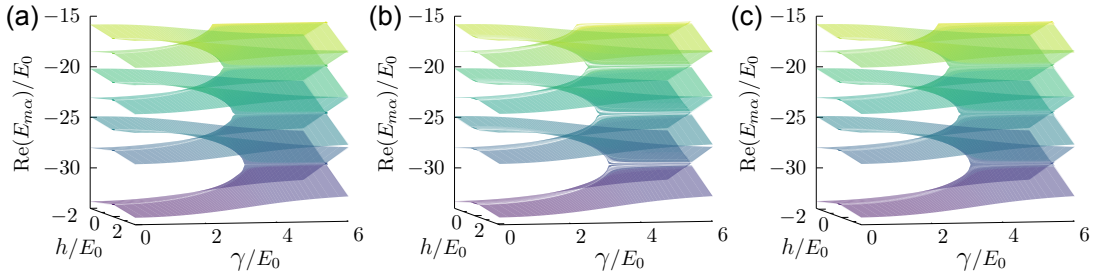


FIG. S1: Riemann structure of real parts of the eigenvalues in the $h - \gamma$ plane for different m . Here, (a) $m = 0$, (b) $m = -1$ and (c) $m = 1$ with fixed $\Omega_0/E_0 = 0.82$. Other parameters are the same as those in Fig. 2.

Full-band expansion

To capture the underlying physics, as discussed in the main text, the eigenspectrum of Hamiltonian (1) can be derived more transparently by reconsidering the non-Hermitian Hamiltonian,

$$H_0 = \int d\mathbf{r} \begin{pmatrix} \psi_{\uparrow}^{\dagger}(\mathbf{r}) & \psi_{\downarrow}^{\dagger}(\mathbf{r}) \end{pmatrix} \begin{pmatrix} K_{\uparrow}(\mathbf{r}) - \omega & \Omega_0 I(r) \\ \Omega_0 I(r) & K_{\downarrow}(\mathbf{r}) + \omega \end{pmatrix} \begin{pmatrix} \psi_{\uparrow}(\mathbf{r}) \\ \psi_{\downarrow}(\mathbf{r}) \end{pmatrix}. \quad (\text{S7})$$

Inspired by Ref. [1, 2], we expand the field operator $\psi_{\sigma}(\mathbf{r})$ in two dimensions as

$$\psi_{\sigma}(\mathbf{r}) = \sum_{m,n} \varphi_{mn\sigma}(r) \Theta_m(\theta) a_{mn\sigma}, \quad (\text{S8})$$

where $\varphi_{mn\sigma}(r)$ satisfies

$$K_{\sigma}(\mathbf{r}) \varphi_{mn\sigma}(r) \Theta_m(\theta) = \epsilon_{mn\sigma} \varphi_{mn\sigma}(r) \Theta_m(\theta), \quad (\text{S9})$$

as shown in the main text. Here, n and m denote the radial and angular quantum numbers, respectively. Specifically, the radial wave function $\varphi_{mn\sigma}(r)$ can be expanded by the radial function of the two-dimensional hard-wall potential,

$$\varphi_{mn\sigma}(r) = \sum_p c_{mn\sigma}^p R_{p,m-l\tau}(r), \quad (\text{S10})$$

where $\tau = +1(-1)$ for $\sigma = \uparrow(\downarrow)$. Substitute Eq. (S10) to Eq. (S9), we have the following equation

$$\sum_{p'} K_{\sigma,m-l\tau}^{pp'} c_{mn\sigma}^{p'} = \epsilon_{mn\sigma} c_{mn\sigma}^p, \quad (\text{S11})$$

where $K_{\sigma,m-l\tau}^{nn'}$ can be found in Eq. (S5). Solving Eq. (S11), $\epsilon_{mn\sigma}$ and the radial wave function of $K_{\sigma}(\mathbf{r})$ can be obtained. Intuitively, when the ac Stark potential becomes steep, i.e., $\chi_0 \ll 0$, a large energy gap emerges between neighboring n levels for a given angular quantum number m . In this scenario, the index n plays a role analogous to the band index, i.e., $n = s, p, d, f, \dots$.

Substitute Eq. (S8) into Eq. (S7), we have $H_0 = \sum_m H_m$, where H_m is given by

$$H_m = \sum_{n\sigma} \left[\epsilon_{mn\sigma} - \omega\tau \right] a_{mn\sigma}^{\dagger} a_{mn\sigma} + \sum_{nn'} \left(\Omega_{n\uparrow, n'\downarrow}^m a_{mn\uparrow}^{\dagger} a_{mn'\downarrow} + h.c. \right), \quad (\text{S12})$$

Here, we define

$$\Omega_{n\sigma, n'\sigma'}^m = \Omega_0 \int r dr \varphi_{mn\sigma} I(r) \varphi_{mn'\sigma'}. \quad (\text{S13})$$

Diagonalizing Eq. (S12) yields the eigenvalues and eigenstates. Figure S2 shows the real and imaginary parts of the eigenspectra in the $m = 0$ sector for $h = 0$ as the Raman coupling Ω_0 increases. As discussed in the main text, for weak Raman coupling, the real dressed bands are well separated, and each hosts an intra-band EP (marked in red) [see

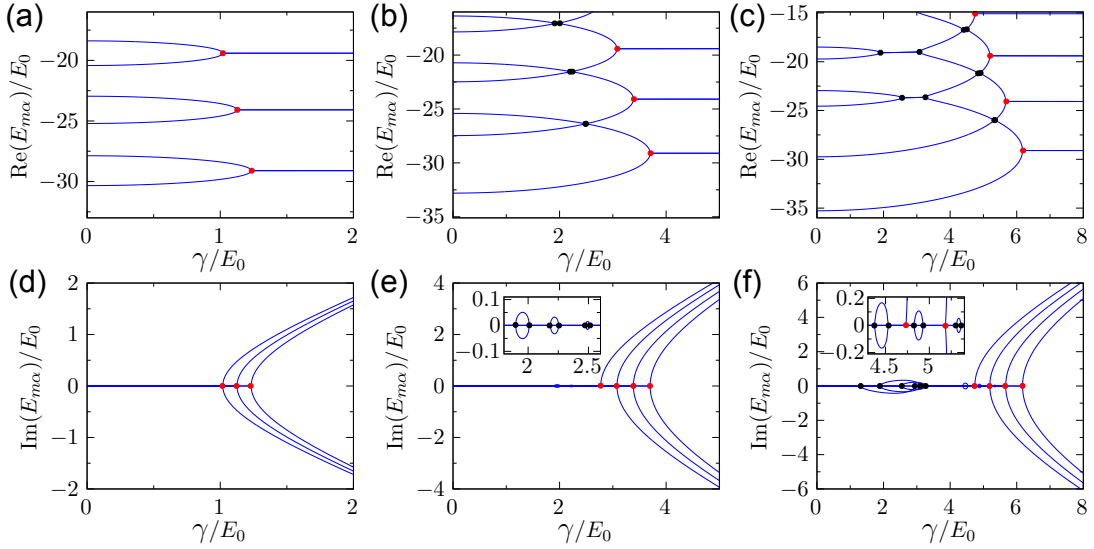


FIG. S2: Real and imaginary parts of the eigenspectra as γ increases for $h = 0$ under different Raman coupling Ω_0 in the $m = 0$ sector. Here, (a)(b)(c) denote the real part of the eigenspectra for $\Omega_0/E_0 = 0.27, 0.82$ and 1.37 . (d)(e)(f) are the corresponding imaginary parts, the inset plots in panels (e) and (f) provide zoomed-in views. Other parameters are the same as those in Fig. 2.

Fig. S2(a)]. As the Raman coupling strength increases, different dressed bands hybridize, leading to the emergence of inter-band EPs [see Fig. S2(b)]. Correspondingly, the number of EPs increases with the coupling strength [see Fig. S2(c)]. Figure S2 also shows the corresponding imaginary dressed bands as the Raman coupling Ω_0 increases, which are consistent with the real-band structures.

Compared with the direct basis expansion, the full-band expansion provides clear physical insight into both the static and dynamical properties; in particular, it enables the derivation of an effective Hamiltonian that elucidates the underlying physics. For example, as discussed in the main text, restricting the expansion to the s and d bands reduces Eq. (S12) to $H_m = \Phi_m^\dagger \mathcal{H}_m \Phi_m$, where

$$\mathcal{H}_m = \begin{pmatrix} \epsilon_{ms\uparrow} - \omega & \Omega_{s\uparrow,s\downarrow}^m & 0 & \Omega_{s\uparrow,d\downarrow}^m \\ \Omega_{s\uparrow,s\downarrow}^m & \epsilon_{ms\downarrow} + \omega & \Omega_{d\uparrow,s\downarrow}^m & 0 \\ 0 & \Omega_{d\uparrow,s\downarrow}^m & \epsilon_{md\uparrow} - \omega & \Omega_{d\uparrow,d\downarrow}^m \\ \Omega_{s\uparrow,d\downarrow}^m & 0 & \Omega_{d\uparrow,d\downarrow}^m & \epsilon_{md\downarrow} + \omega \end{pmatrix}, \quad (\text{S14})$$

and $\Phi_m = (a_{ms\uparrow} \ a_{ms\downarrow} \ a_{md\uparrow} \ a_{md\downarrow})^T$. Retaining only the n th term yields the one-band approximation, in which case, Eq. (S12) reduces to $H_m = \Phi_m^\dagger \mathcal{H}_m \Phi_m$, where

$$\mathcal{H}_m = \begin{pmatrix} \epsilon_{mn\uparrow} - \omega & \Omega_{n\uparrow,n\downarrow}^m \\ \Omega_{n\uparrow,n\downarrow}^m & \epsilon_{mn\downarrow} + \omega \end{pmatrix}, \quad (\text{S15})$$

and $\Phi_m = (a_{mn\uparrow} \ a_{mn\downarrow})^T$. When we focus on the $m = 0$ sector, Eq. (S14) and (S15) reduce to Eq. (7) and (8) in the main text. These effective Hamiltonians capture both the static and dynamical properties of the system.

CHIRAL DYNAMICAL FORMALISM

The chiral dynamics are studied via the time-dependent Schrödinger equation, $i\hbar\partial_t\psi = \mathcal{H}_s(t)\psi$, where

$$\mathcal{H}_s(t) = \sum_{\sigma} K_{\sigma}(\mathbf{r}) + \Omega_0 I(r)\sigma_x - \omega(t)\sigma_z, \quad (\text{S16})$$

with $\omega(t) = h(t) - i\gamma(t)$. Since $[L_z, \mathcal{H}_s(t)] = 0$, we expand $\psi_{\sigma}(\mathbf{r}, t) = \sum_{m,n} \varphi_{m\sigma}(r)\Theta_m(\theta)a_{mn\sigma}(t)$, which reduces the dynamics to $i\hbar\partial_t\Phi_m(t) = \mathcal{H}_m(t)\Phi_m(t)$, as $\mathcal{H}_s(t)$ decouples into independent m sectors. Here $\mathcal{H}_m(t)$ is the

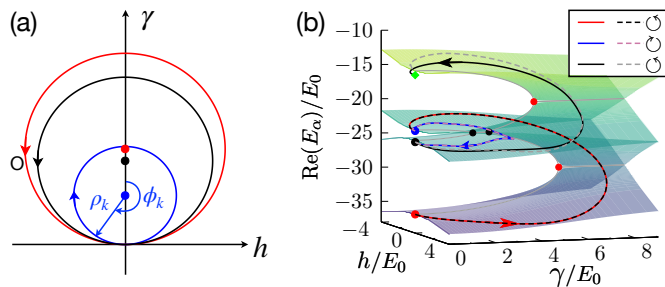


FIG. S3: Comparison of adiabatic encircling results from the two-band and full-band models. (a) Schematic of the designed loops. (b) Spectral trajectories of the encircling. The solid lines denote the results from the effective two-band model, while the dashed lines correspond to the full-band calculation. Here, $\Omega_0/E_0 = 1.37$. Other parameters are the same as those in Fig. 2 and Fig. 5.

instantaneous non-Hermitian Hamiltonian in the m sector and $\Phi_m(t)$ is the corresponding time-evolved state, with explicit expressions for both given by

$$\mathcal{H}_m(t) = \begin{pmatrix} \epsilon_{ms\uparrow} - \omega(t) & \Omega_{s\uparrow,s\downarrow}^m & 0 & \Omega_{s\uparrow,p\downarrow}^m & \cdots \\ \Omega_{s\uparrow,s\downarrow}^m & \epsilon_{ms\downarrow} + \omega(t) & \Omega_{p\uparrow,s\downarrow}^m & 0 & \cdots \\ 0 & \Omega_{p\uparrow,s\downarrow}^m & \epsilon_{mp\uparrow} - \omega(t) & \Omega_{p\uparrow,p\downarrow}^m & \cdots \\ \Omega_{s\uparrow,p\downarrow}^m & 0 & \Omega_{p\uparrow,p\downarrow}^m & \epsilon_{ms\downarrow} + \omega(t) & \cdots \\ \cdots & \cdots & \cdots & \cdots & \ddots \end{pmatrix}, \quad (\text{S17})$$

and $\Phi_m(t) = (a_{ms\uparrow}(t) \ a_{ms\downarrow}(t) \ a_{mp\uparrow}(t) \ a_{mp\downarrow}(t) \ \cdots)^T$, where the definition of $\epsilon_{mn\sigma}$ and $\Omega_{n\sigma,n'\sigma'}$ can be found in Eq. (S9) and (S13). Thus, given an initial state $\Phi_m(0)$ and the time evolution of $\omega(t)$, the time-evolved state $\Phi_m(t)$ can be obtained.

As discussed in the main text, we focus on the $m = 0$ sector. In this case, $\mathcal{H}_m(t)$ and $\Phi_m(t)$ reduces to

$$\mathcal{H}(t) = \begin{pmatrix} \epsilon_{s\uparrow} - \omega(t) & \Omega_{s\uparrow,s\downarrow} & 0 & \Omega_{s\uparrow,p\downarrow} & \cdots \\ \Omega_{s\uparrow,s\downarrow} & \epsilon_{s\downarrow} + \omega(t) & \Omega_{p\uparrow,s\downarrow} & 0 & \cdots \\ 0 & \Omega_{p\uparrow,s\downarrow} & \epsilon_{p\uparrow} - \omega(t) & \Omega_{p\uparrow,p\downarrow} & \cdots \\ \Omega_{s\uparrow,p\downarrow} & 0 & \Omega_{p\uparrow,p\downarrow} & \epsilon_{s\downarrow} + \omega(t) & \cdots \\ \cdots & \cdots & \cdots & \cdots & \ddots \end{pmatrix}, \quad (\text{S18})$$

and $\Phi(t) = (a_{s\uparrow}(t) \ a_{s\downarrow}(t) \ a_{p\uparrow}(t) \ a_{p\downarrow}(t) \ \cdots)^T$. Here, we have omitted the angular quantum number for simplicity.

COMPARISONS OF ADIABATIC ENCIRCLING

For the adiabatic encircling discussed in the main text, we compare the spectral trajectories obtained from the effective two-band model with those from the full-band calculation. As illustrated in Fig. S3, the two results show excellent agreement, particularly for short encircling times t . For large t , deviations emerge due to the increasing importance of higher-band contributions, which lie beyond the two-band description.

* Electronic address: chenkeji2010@gmail.com

† Electronic address: t21060@fzu.edu.cn

‡ Electronic address: wyz@ustc.edu.cn

- [1] L.-L. Wang, A.-C. Ji, Q. Sun, and J. Li, Exotic Vortex States with Discrete Rotational Symmetry in Atomic Fermi Gases with Spin-Orbital–Angular-Momentum Coupling, *Phys. Rev. Lett.* **126**, 193401 (2021).
 [2] K.-J. Chen, F. Wu, L. He, and W. Yi, Angular topological superfluid and topological vortex in an ultracold Fermi gas, *Phys. Rev. Res.* **4**, 033023 (2022).